

# Coherent manipulation of interacting electron qubits on solid neon

Xinhao Li,<sup>1,2, a)</sup> Yizhong Huang,<sup>2,3</sup> Xu Han,<sup>2,3</sup> Xianjing Zhou,<sup>4,5, b)</sup> and Dafei Jin<sup>6, c)</sup>

<sup>1)</sup>Department of Physics, Harvard University, Cambridge, Massachusetts 02138, USA

<sup>2)</sup>Center for Nanoscale Materials, Argonne National Laboratory, Lemont, Illinois 60439, USA

<sup>3)</sup>Pritzker School of Molecular Engineering, University of Chicago, Chicago, Illinois 60637, USA

<sup>4)</sup>National High Magnetic Field Laboratory, Tallahassee, Florida 32310, USA

<sup>5)</sup>Department of Mechanical Engineering, FAMU-FSU College of Engineering, Florida State University, Tallahassee, Florida 32310, USA

<sup>6)</sup>Department of Physics and Astronomy, University of Notre Dame, Notre Dame, Indiana 46556, USA

(Dated: 4 August 2025)

**Solid neon has emerged as a pristine material host for electron qubits.** Single electron-on-solid-neon (eNe) charge qubits have shown extraordinarily long coherence times and high operation fidelities. Realizing two-qubit gates in this platform is the next major step for realistic quantum information processing. In this work, we demonstrate frequency- and time-domain coherent manipulation of multiple eNe charge qubits that are coupled by charge interactions. Cross-resonance and bSWAP two-qubit gates are implemented, laying the foundation for universal quantum computing. An inter-qubit coupling strength exceeding 60 MHz has been observed, promising fast gate speed and suppressed infidelity. These results highlight the potential to scale up the eNe qubit platform toward universal quantum computing.

Electrons on solid neon (eNe) is an emerging solid-state qubit platform<sup>1–4</sup>. Qubits based on charge states of eNe have shown great coherence performance and high-fidelity single-qubit operation because of the robust electron host environment offered by the neon layer<sup>2</sup>. Meanwhile, the directness of charge qubits in terms of control and detection via electrical fields can largely simplify circuit design in a system with high qubit volume. To scale up charge qubits on solid neon, it is essential to demonstrate coherent interactions between them<sup>4,5</sup>. In semiconductor electron hosts, strong coupling between qubits has been established through charge interactions at short distances<sup>6–8</sup>, which showcased the advantage of electron qubits in large-number integration on a small chip<sup>9,10</sup>. For electrons on cryogenic substrates, charge interactions have also been proposed to perform two-qubit gates and generate entanglements<sup>4,11,12</sup>.

Previously, we have observed the case of multiple electron qubits loaded onto a single niobium superconducting resonator<sup>2</sup>. Although the two qubits simultaneously achieved strong coupling with the cavity, the inter-qubit coupling strength is small, which prevents the demonstration of two-qubit operations. This observation has demonstrated the possibility of forming multiple electron traps on the neon surface during its solidification. Recent theoretical and experimental studies have highlighted the

critical role of neon surface roughness in trapping electron qubits and shaping their properties<sup>13–15</sup>. When two qubits are located close to each other in the traps formed on the rough neon surface, the charge interaction with a strength surpassing the qubits' decoherence would enable coherent two-qubit operations. Therefore, it is straightforward to pursue coherent local coupling between qubits on solid neon to demonstrate its scalability. It may also offer a unique testbed for studying the entanglement of electrons in free space and for the simulation of many-body quantum systems<sup>16,17</sup>.

In this work, we achieve the coherent manipulation of multiple interacting electron qubits on solid neon in the circuit quantum electrodynamics architecture (cQED)<sup>18,19</sup>. Qubit spectroscopy measurements show strong coupling between two qubits on solid neon with an interaction strength of  $J/2\pi = 3.35$  MHz. Further, by driving one of the two qubits, which is strongly coupled with the superconducting resonator, we are able to demonstrate cross-resonance (CR) and bSWAP types of all-microwave two-qubit operations<sup>20</sup>. The experiment results match well with theoretical simulations of the two-qubit coupled system based on characterized parameters. Additionally, we observe even stronger coupling in a three-qubit system, with a maximum interaction strength of  $J/2\pi = 62.5$  MHz. These results demonstrate coherent interactions between qubits on solid neon, laying the foundation for scaling up the system toward applications in quantum computing and simulation.

## Multi-qubit systems

We utilize a cQED architecture to drive and read out charge qubits on solid neon coupled with microwave photons within a superconducting resonator. Specifically, multiple qubits could exist on the neon film near the designed electron trapping area, as shown in Fig. 1a, whose coupling strength with the resonator is determined by the alignment between the qubits' dipole moments and the local microwave electrical field. For two closely arranged qubits  $Q_i$  and  $Q_j$ , they can directly couple with each other through charge interactions. The generalized system Hamiltonian, considering both transverse and longitudinal qubit interactions, can be written as

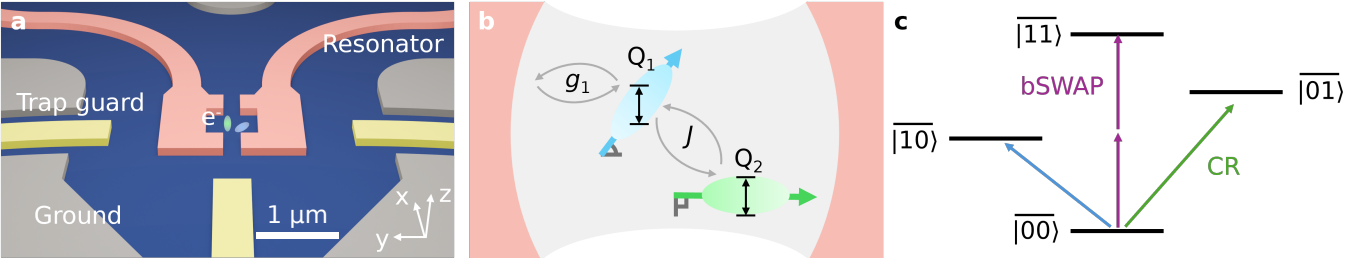


**Fig. 1. Schematic of multi-qubit coupling on neon-covered superconducting resonator.** **a**, Two closely arranged qubits trapped at the open end of a splitting co-planar waveguide superconducting resonator, surrounded by electrical gates. In our experiment, varying gate voltage is symmetrically applied on the left and right trap guards ( $\Delta V_{\text{tg}}$ ) or on the resonator pins ( $\Delta V_{\text{res}}$ ) to tune the qubits' transition frequency. **b**, Schematic of the interactions between qubits and the superconducting resonator, where  $Q_1$  and  $Q_2$  are coupled with strength  $J$  and  $Q_1$  is coupled to the resonator with strength  $g$ . **c**, Energy level schematic of the two-qubit system showing possible transitions.

$$\begin{aligned} \hat{H}_{\text{sys}} &= \hat{H}_{\text{r}} + \hat{H}_{\text{q}} + \hat{H}_{\text{int}} \\ \hat{H}_{\text{r}} &= \hbar\omega_{\text{r}}\hat{a}^\dagger\hat{a} \\ \hat{H}_{\text{q}} &= \sum_i \frac{1}{2}\hbar\omega_i\hat{\sigma}_i^z \\ \hat{H}_{\text{int}} &= \sum_i \hbar g_i(\hat{a}^\dagger\hat{\sigma}_i^- + \hat{a}\hat{\sigma}_i^+) \\ &\quad + \sum_{ij} \hbar J_{ij}(\hat{\sigma}_i^+\hat{\sigma}_j^- + \hat{\sigma}_i^-\hat{\sigma}_j^+) \\ &\quad + \sum_{ij} \hbar\zeta_{ij}(\hat{\sigma}_i^z\hat{\sigma}_j^z) \end{aligned} \quad (1)$$

where  $\hat{H}_{\text{r}}$ ,  $\hat{H}_{\text{q}}$ , and  $\hat{H}_{\text{int}}$  are the resonator, qubits, and interaction Hamiltonians.  $\omega_{\text{r}}$  is the resonator frequency,  $\omega_i$  is the transition frequency of  $Q_i$ ,  $g_i$  is the coupling strength between the resonator and  $Q_i$ ,  $J_{ij}$  ( $\zeta_{ij}$ ) represents the transverse (longitudinal) inter-qubit coupling strength between  $Q_i$  and  $Q_j$ .  $\hat{a}$  and  $\hat{a}^\dagger$  are the annihilation and creation operators of resonator photons.  $\hat{\sigma}_i^z$ ,  $\hat{\sigma}_i^-$ , and  $\hat{\sigma}_i^+$  are the Pauli- $z$ , lowering, and raising operators acting on  $Q_i$ . The system is driven by microwaves with a time-dependent amplitude  $A(t)$  and frequency  $\omega_{\text{d}}$ , and the driving Hamiltonian can be written as

$$\hat{H}_{\text{d}} = A(t)\cos(t\omega_{\text{d}}) \sum_i \hbar\eta_i(\hat{\sigma}_i^+ + \hat{\sigma}_i^-), \quad (2)$$

where  $\eta_i$  is the ratio for direct driving on  $Q_i$  (ref. <sup>21</sup>).

Because of the disordered neon surface, two closely arranged qubits may have distinct coupling strengths with the superconducting resonator, depending on their dipole orientation<sup>18,22</sup>. As shown in Fig. 1b, inside a two-qubit coupled system,  $Q_2$  with a dipole moment orthogonal to the MW field within a superconducting cavity could result in a close to zero qubit-cavity coupling strength. In such a case, if  $Q_1$  is coupled with the resonator via a finite dipole alignment, and  $Q_1$  is

interacting with  $Q_2$  at a strength  $J$ , we will have a system Hamiltonian with  $g_2 \sim 0$ ,  $\eta_1 \sim 1$  and  $\eta_2 \sim 0$  (ref. <sup>21</sup>).

Such a two-qubit system could support all-microwave-driven two-qubit operations, including the cross-resonance (CR) and bSWAP types of two-qubit gates, as shown in Fig. 1c. All-microwave two-qubit gates are widely applied to fixed-frequency qubits thanks to their easy implementation, which also preserves the qubits' coherence by avoiding electrostatic and flux gating<sup>20</sup>. In CR gates,  $Q_2$  is excited by driving  $Q_1$  at the frequency of  $Q_2$ , generating the transition  $|00\rangle \rightarrow |01\rangle$  (refs. <sup>23–25</sup>). In bSWAP gates,  $Q_1$  and  $Q_2$  are driven monochromatically through a two-photon process near the frequency middle point between them, generating the transition  $|00\rangle \rightarrow |11\rangle$  (refs. <sup>21,26</sup>).

## Two-qubit strong coupling

We have achieved the strong coupling between two qubits on solid neon. Figure 2a plots the two-tone measured qubit spectroscopy, in which we probe the system at the resonator frequency with low power, approximately -130 dBm reaching the resonator's input coupler, while sending a second continuous-wave tone with scanning frequency. Two clear avoided crossings are observed while tuning the bias voltage on the trap guard electrode ( $\Delta V_{\text{tg}}$ ), with a splitting magnitude of  $J/2\pi = 3.35$  MHz, larger than the linewidth of the hybrid states above and below the splitting, as shown in Fig. 2b. This indicates the strong coupling between a qubit ( $Q_1$ ), which is visible in the two-tone spectroscopy, and another “dark” one ( $Q_2$ ).

Individually,  $Q_1$  has a hyperbolic frequency dependency on  $\Delta V_{\text{tg}}$ , with a charge sweet-spot (SS) located near 5.71 GHz, which is about 40 MHz above the resonator frequency at 5.668 GHz. The coupling between  $Q_1$  and the resonator dispersively pushes the resonator spectrum, especially when  $Q_1$  is tuned to its SS frequency, as shown in the Supplementary Information. Based on this, we estimate the coupling strength between  $Q_1$  and the resonator to be  $g_1/2\pi = 3.76$  MHz.

In contrast, the interaction between  $Q_2$  and the

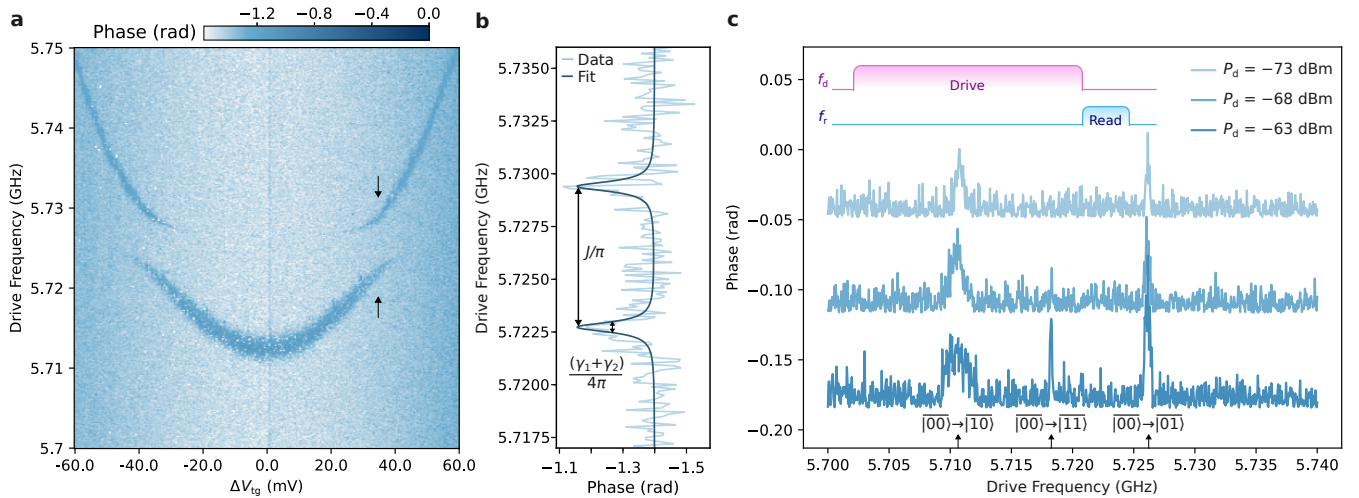


**Fig. 2. Spectroscopic characterization of coherent two-qubit coupling on solid neon.** **a**, Two-tone qubit spectroscopy with avoided splittings. **b**, Line cut of the two dressed states, at the black arrows in a, with splitting magnitude of  $J/2\pi = 3.35$  MHz. **c**, Qubits spectroscopy measured with high-power pulsed readout. Driving pulse power ( $P_d$ ) reaching the resonator's input coupler was increased from  $-73$  dBm to  $-63$  dBm, activating transitions corresponding to the CR and bSWAP two-qubit operations. The measurements were taken when system was biased at  $\Delta V_{tg} = 0$  V. The phase curves are off-set for visualization.

superconducting resonator is much weaker than that of  $Q_1$ . Meanwhile, the secondary shift of the resonator caused by the dispersive push of  $Q_2$  on  $Q_1$  is also small. Together, these lead to a negligible  $Q_2$ -state-dependent shift of the resonator frequency and the absence of visible  $Q_2$  spectroscopy in Fig. 2a. In addition, the spectroscopic symmetry of the two avoided crossing in against  $\Delta V_{tg}$  indicates that the frequency of  $Q_2$  is much less sensitive to  $\Delta V_{tg}$  compared to that for  $Q_1$ , with a nearly constant frequency of 5.726 GHz in the voltage scanning range of Fig. 2a. These observations all suggest the misalignment between  $Q_2$ 's dipole and the microwave and direct current (DC) gating fields.

We attribute the two-qubit coupling to charge interactions at short distances. The spectroscopic observations reveal a coupled two-qubit system represented in Fig. 1b, with finite  $g_1$  but  $g_2 \sim 0$  and  $\eta_2 \sim 0$  of Eq. (1) and (2). Due to the distinct coupling strengths between the two qubits and the resonator, we can rule out the case that the two qubits achieved strong coupling via virtual microwave photon exchange through the resonator, in which the inter-qubit exchange strength  $J = g_1 g_2 (1/\Delta_1 + 1/\Delta_2)/2$ , where  $\Delta_{1,2}$  are the detune between the qubits and the resonator<sup>27</sup>.

Despite the fact that only  $Q_1$  has a strong interaction with the superconducting resonator, we have managed to probe  $Q_2$  utilizing the inter-qubit coupling. When probing the system with a readout pulse, the resonator will be populated with an average intra-cavity photon number  $\bar{n}$ , which will induce a blue ac-Stark shift of  $Q_1$  at  $2\bar{n}\chi$ <sup>2,19</sup>. Due to the undetectable coupling between  $Q_2$  and the resonator, the probe signal will not affect  $Q_2$  directly. Given the dispersive coupling strength of  $\chi/2\pi \approx 0.33$  MHz,  $Q_1$ 's frequency can shift across  $Q_2$ 's

frequency approximately at  $\bar{n} \sim 20$ . Therefore, the pulsed probe can act as a SWAP operation between  $Q_1$  and  $Q_2$  (ref. <sup>27</sup>), which eventually results in a  $Q_2$ -state-dependent readout at the resonator frequency. This effect is turned off when the probe tone is weak, as in case of Fig. 2a. See Supplementary Information for example simulations of the pulsed readout process.

With this method, we perform pulsed qubit spectroscopy when biased at  $Q_1$ 's SS. A long square pulse (10  $\mu$ s) with varying frequency and driving power is first applied to saturate the system to a specific state, followed by a short square probe pulse (700 ns) at the resonator frequency with approximately -120 dBm reaching the resonator. The pulse sequence is shown in the inset of Fig. 2c. At low driving power, we observe two transitions at 5.711 GHz and 5.726 GHz, corresponding to frequencies of  $Q_1$  at its SS and  $Q_2$ . The appearance of  $|00\rangle \rightarrow |01\rangle$  transition indicates that the long driving pulse saturated  $Q_2$  to a certain population, corresponding to the CR transition of a two-qubit coupled system<sup>23,25</sup> in Fig. 1c. With the increase in the driving power, we observe another transition peak ( $|00\rangle \rightarrow |11\rangle$ ) nearly at the middle of the  $Q_1$  and  $Q_2$  frequencies of 5.7185 GHz. This corresponds to the bSWAP type of two-qubit operation in Fig. 1c, involving two-photon excitation<sup>21,26</sup>. The fact that  $\omega_{|11\rangle} - \omega_{|01\rangle} - \omega_{|10\rangle} \simeq 0$  suggests the effective longitudinal (ZZ) interaction in the system is small<sup>11,28</sup>. In summary, through spectroscopic characterization, we have observed the coherent coupling between two qubits on solid neon, which can support both the CR and the bSWAP types of two-qubit operation.

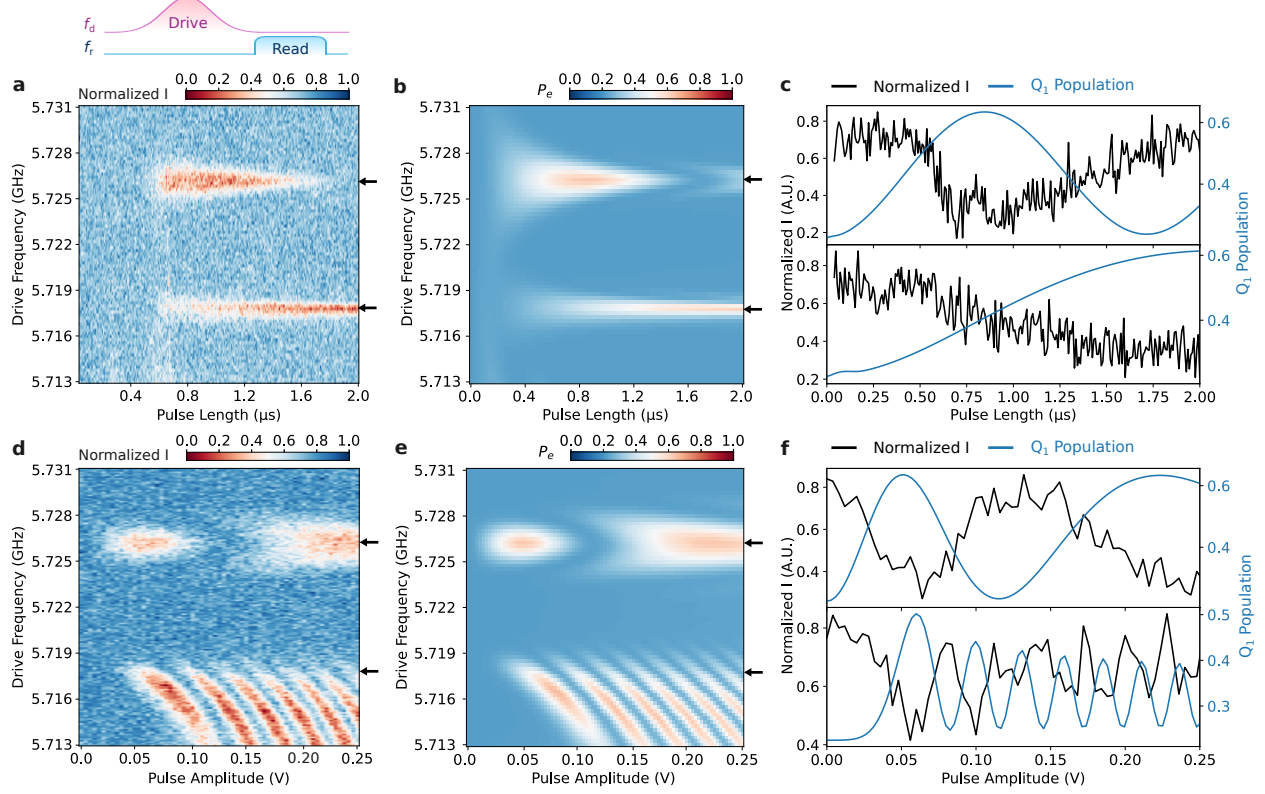


**Fig. 3. Time-domain all-microwave two-qubit operations on solid neon.** **a** and **d**, Pulse length-frequency (a) and pulse amplitude-frequency (d) Rabi measurements, following the pulse sequences in the inset, showing the two operations corresponding to cross-resonance (CR, top arrows) and bSWAP (bottom arrows) two-qubit gates. **b** and **e**, Simulated Q<sub>1</sub> excited state population after the readout pulse in pulse length-frequency (b) and pulse amplitude-frequency (e) Rabi measurements. **c** and **f**, Experiment recorded readout signal and numerically simulated Q<sub>1</sub> population after readout. Data in Fig. 3c (3f) are adopted from line cuts at the arrows in Fig. 3a-b (3d-e), corresponding to CR (top plots) and bSWAP (bottom plots) operations.

## Two-qubit gate operation

Following spectroscopic characterization of the coupled system, we perform time-domain two-qubit operations corresponding to the CR and bSWAP gates. Figure 3a plots the readout signal following Gaussian-shaped driving pulses with varying lengths and approximately -70 dBm reaching the resonator input coupler. The driving pulses are truncated at  $\pm 2.5\sigma$  on each side, where  $\sigma$  is the standard deviation of the Gaussian envelope. The parameters of the readout pulses are the same as described in the last section. Two oscillation features corresponding to the CR operation near 5.726 GHz and the bSWAP operation near 5.718 GHz can be observed. Based on the system Hamiltonian, we numerically simulate<sup>29</sup> the qubits' excited state population during the pulse-driving and after the readout process, as shown in Fig. S4 and Fig. 3b, respectively. Due to the readout pulse, Q<sub>2</sub> excited via the two-qubit operation can be reflected in the Q<sub>1</sub> population after the pulse, as shown in Fig. 3b, and consequently, the recorded readout signal. The simulation results in Fig. S4 and Fig. 3b match well with the experiment features in Fig. 3a.

The black solid lines in Fig. 3c plot the two line cuts (corresponding to the arrows in Fig. 3a) of the experiment readout signal at the CR (top subplot) and bSWAP (bottom plot) operation, respectively. The blue curves plot the simulated Q<sub>1</sub> excited state population after the readout pulse. In the CR operation, Q<sub>2</sub> was driven by pumping Q<sub>1</sub> at the transition frequency of Q<sub>2</sub>, whose excited state population reached maximum when the pulse length was approximately 0.8  $\mu$ s. On the other hand, Q<sub>1</sub> was barely excited in the CR operation, as shown in Fig. S4.

In the bSWAP operation, the two-photon process drives the two qubits simultaneously, as shown in Fig. S4, while the oscillation frequency is much lower than the CR operation. Under a square driving pulse with amplitude  $A$ , and negligible direct driving on the Q<sub>2</sub>, the oscillation frequency induced by CR operation is  $\Omega_{\text{CR}} = AJ/(\Delta_{12} + 2J^2/\Delta_{12})$  (ref. <sup>23</sup>). In bSWAP operation, the oscillation frequency is approximately  $\Omega_{\text{bSWAP}} = 2A^2J/(\Delta_{12} + 2J^2/\Delta_{12})^2$  (ref. <sup>21</sup>), where  $\Delta_{12}$  is the frequency separation between Q<sub>1</sub> and Q<sub>2</sub>. When the bSWAP operation performs a  $\pi$  rotation, which is about 2  $\mu$ s in our case, it is locally equivalent to an iSWAP gate

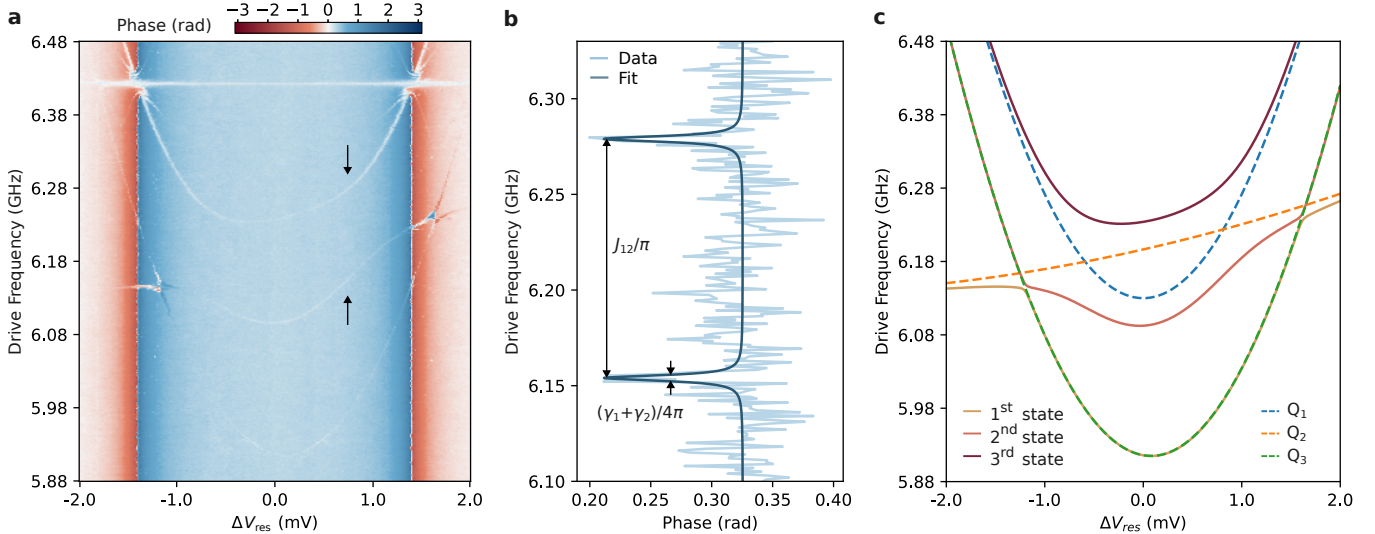


**Fig. 4. Spectroscopic characterization of a three-qubit coupled system on solid neon.** **a**, Two-tone measured qubits spectroscopy showing three-qubit coupled system **b**, The line cut showing large coupling strength between  $Q_1$  and  $Q_2$  of  $J_{12}/2\pi = 62.5$  MHz. **c**, Calculated eigenstate energy diagram of the three-qubits coupled system, with undressed qubit states shown as dashed lines.

with appropriate single-qubit rotations<sup>21</sup>.

Additionally, we perform pulse amplitude-dependent Rabi oscillation measurement with a Gaussian-shaped driving pulse of 800 ns length and output pulse amplitude varying from 0.0 V to 0.25 V, corresponding to zero power to -57 dBm reaching the resonator input coupler. Again, we observe oscillating patterns near 5.726 GHz and 5.718 GHz, corresponding to the CR and bSWAP operations. We attribute the “waterfall-like” patterns in the frequency range between 5.713 - 5.718 GHz in Fig. 3d to the effects of the Gaussian pulse shape and the ac-Stark shift of  $Q_1$  under higher driving power, which are reproduced by simulations in Fig. 3e and Fig. S4. See detailed discussion in the Supplementary Information. In Fig. 3f, the line cuts at those two driving frequencies matched well with the numerically simulated  $Q_1$  population.

These results demonstrate, for the first time, two-qubit operations on a solid neon platform, revealing the potential for scaling up quantum systems based on charge qubits on solid neon. Further optimization of the two-qubit gate and readout is crucial to achieving high-fidelity operations.

### Three-qubit strong coupling

To further demonstrate the scalability via charge interactions, we have managed to create a system with three qubits on solid neon. Figure 4a plots the two-tone measured qubit spectrum while varying the gate voltage on the resonator electrode ( $\Delta V_{\text{res}}$ ), revealing the energy diagram of this three-qubit system. One of them ( $Q_1$ ) is directly coupled with a superconducting resonator, while the other two ( $Q_2$  and  $Q_3$ ) are serially coupled to  $Q_1$ . Compared to  $Q_1$ , the interactions strengths of

$Q_2$  and  $Q_3$  with the resonator are weak. We do not observe the vacuum Rabi splitting between them and the resonator. Besides, the dispersive phase shift of the resonator induced by  $Q_2$  and  $Q_3$  is also small when they are not hybridized with  $Q_1$ .

In Fig. 4b, the line cut around  $\Delta V_{\text{res}} = 0.74$  mV shows a coupling strength of  $J_{12}/2\pi = 62.5$  MHz between  $Q_1$  and  $Q_2$ . On the other hand, the coupling strength  $J_{23}/2\pi$  between  $Q_2$  and  $Q_3$  is much smaller, at approximately 5 MHz level. Due to the weak interaction between  $Q_{2,3}$  and the resonator, we attribute the three-qubit coupling to charge interactions instead of virtual photon exchange via the resonator.

Figure 4c plots the calculated eigenstates of the system, which match well with the two-tone spectroscopy.  $Q_1$  and  $Q_2$  have closely arranged SS near 6.13 GHz, while  $Q_3$ ’s SS is more detuned to approximately 5.91 GHz. All three qubits are responsive to the bias voltage on the resonator electrode with various sensitivities. See details in the Supplementary Information for those parameters applied in the calculation. Due to the strong coupling strength between  $Q_1$  and  $Q_2$ , the state mixing of the three qubits results in the energy diagram of the coupled system, which deviates from the undressed qubit spectrum. As a result, the three mixed states are all visible in the two-tone measurement in Fig. 4a. These observations indicate the possibilities of creating multi-qubit coupled systems on solid neon that may be applied for small- to middle-scale quantum simulations<sup>16,17</sup>.

### Discussion and outlook

In this work, we have realized coherently interacting multiple qubits on solid neon, mediated by charge interactions. In a two-qubit system, both spectroscopic

avoided crossing and time-domain pulse operations have demonstrated coherent qubit interactions. Cross-resonance and bSWAP two-qubit operations have been demonstrated, paving the way for the optimization of high-fidelity two-qubit gates on solid neon. Further, a three-qubit system with over 60 MHz inter-qubit coupling strength shows the potential of building more complex systems with qubits on solid neon.

Charge interactions between qubits at short distances may enable new possibilities for quantum information processing on solid neon. In the two systems studied in this work, qubits can acquire distinct coupling strengths with superconducting resonators. Utilizing such possibilities, qubits with dipole moments oriented normal to the resonator field can serve as quantum memories for nearby coupled qubits<sup>30,31</sup>, or act as intermediate quantum buses<sup>32</sup>. The variation in qubit-resonator coupling strengths further reflects the complexity of electron trapping on solid neon films and points to the important role of surface profile in determining qubit properties<sup>13–15,33</sup>.

Establishing coherent charge interactions between adjacent qubits on solid neon is a crucial step toward scaling up this emerging solid-state qubit platform. However, a multi-qubit system purely relying on charge interactions at short distance will pose challenges to integrated control and read-out circuits. Entanglement between distant qubits through superconducting cavity buses could ease the limits in local interactions<sup>27,34–36</sup>. High-impedance resonators made of high-kinetic inductance thin films<sup>37,38</sup> and Josephson junction arrays<sup>39,40</sup> have been applied to achieve coherent interactions between distant semiconductor qubits. Further improvements in the control of individual qubit properties above solid neon with refined film growth, electron trapping and gating mechanisms, as well as the development of a compatible high-impedance resonator<sup>41,42</sup> would facilitate remote entanglements between distant qubits and hybridize it with other quantum platforms<sup>31,43</sup>. Looking ahead, the integration of short- and long-distance interactions between qubits on solid neon could pave the way for an on-chip quantum network.

## Methods

### Devices and experiments

The data presented in Fig. 1 and 2 were collected on a high-impedance titanium nitride (TiN) splitting superconducting resonator, the same as the one in ref.<sup>14</sup>. The resonator supports a differential mode at 5.668 GHz with a total linewidth of  $\kappa/2\pi = 0.38$  MHz. Electrodes with on-chip low-pass filters are connected to the resonator pins and trap guards surrounding the electron-trapping area to apply bias voltages for tuning qubits transition frequency. The device was mounted on a home-made printed circuit board (PCB), sealed in a copper cell with neon filling lines, tungsten filament, and electrical connectors on top of the cell lid. The

cryogenic and room temperature electronics setups are the same as those in ref.<sup>14</sup>. The data presented in Fig. 3 were collected on a niobium splitting superconducting resonator, the same as the one in ref.<sup>1,2</sup>. The resonator supports a differential mode at 6.426 GHz, with a total linewidth of  $\kappa/2\pi = 0.46$  MHz. The sample mounting, cryogenic and room temperature electronic setups were the same as those in refs.<sup>1,2</sup>.

The neon growth procedure is the same as that described in ref.<sup>14</sup>. In summary, the dilution fridge is warmed up to create a temperature gradient from  $\sim 27$  K to  $\sim 25$  K between its 4 K plate and mixing chamber (MXC) plate. At that moment, neon gas is supplied from a room-temperature gas handling system in the form of puffs and filled onto the device chip in the form of liquid. After a desired amount of neon filling, the fridge heater is turned off to let the fridge cool down to base temperature.

Electrons are deposited on to the chip by sending pulsed current on to the tungsten filaments mounted above the device chip. During the electron firing process, temperature sensed on the MXC plate can increase up to 100 mK. The details of the procedure and discussion of the electron deposition process can be found in ref.<sup>14</sup>

### Simulation of multi-qubit coupled system

The populations of qubits in coupled systems are simulated based on their Hamiltonian, using the QuTiP package<sup>29</sup>. For the numerical data presented in Fig. 3, we use Eq. 1 and 2 as the Hamiltonian, with parameters listed in the Supplementary Information. The Lindblad master equation is applied to model the effects of relaxation and dephasing:

$$\begin{aligned} \frac{d\hat{\rho}}{dt} = & -\frac{i}{\hbar}[\hat{H}, \hat{\rho}] \\ & + \frac{\kappa}{2}(2\hat{a}\hat{\rho}\hat{a}^\dagger - \hat{a}^\dagger\hat{a}\hat{\rho} - \hat{\rho}\hat{a}^\dagger\hat{a}) \\ & + \sum_i \frac{\Gamma_i}{2}(2\hat{\sigma}_i^-\hat{\rho}\hat{\sigma}_i^+ - \hat{\sigma}_i^+\hat{\sigma}_i^-\hat{\rho} - \hat{\rho}\hat{\sigma}_i^+\hat{\sigma}_i^-) \\ & + \sum_i \frac{\Gamma_i^\Phi}{2}(2\hat{\sigma}_i^+\hat{\sigma}_i^-\hat{\rho}\hat{\sigma}_i^+\hat{\sigma}_i^- - (\hat{\sigma}_i^+\hat{\sigma}_i^-)^2\hat{\rho} - \hat{\rho}(\hat{\sigma}_i^+\hat{\sigma}_i^-)^2) \end{aligned} \quad (3)$$

where  $\hat{H} = \hat{H}_{\text{sys}} + \hat{H}_{\text{d}}$ .  $\hat{\rho}$  is the system density matrix.  $1/\Gamma_i$  is the relaxation lifetime  $T_1$  of  $Q_i$ , and  $2/\Gamma_i^\Phi$  is the pure dephasing lifetime  $T_\Phi$  of  $Q_i$ , which are adopted from relaxation and Ramsey measurements as shown in the Supplementary Information.

To simulate the readout process, we introduce the Hamiltonian of the probing ( $\hat{H}_p$ ) at the resonator to the system Hamiltonian in the rotating frame as:

$$\hat{H}_p = \epsilon\hbar(\hat{a}^\dagger + \hat{a}), \quad (4)$$

where  $\epsilon$  is the probing amplitude.

## Data availability

The data that support the findings of this study are available from the corresponding authors upon request. Source data are provided with this paper.

## Code availability

The codes used to perform the experiments and to analyze the data in this work are available from the corresponding authors upon request.

## ACKNOWLEDGMENTS

D. J. and X. L. acknowledge support from the Air Force Office of Scientific Research (AFOSR) under Award No. FA9550-23-1-0636 for device fabrication and personnel effort. D. J., X. Z., and Y. H. acknowledge support from the Julian Schwinger Foundation for Physics Research for instrument development. D. J. acknowledges support from the Department of Energy (DOE) under Award No. DE-SC0025542 for solid-neon growth and characterization. D. J. acknowledges support from the National Science Foundation (NSF) under Award No. OSI-2426768 for electron-on-solid-neon structural modeling. Work performed at the Center for Nanoscale Materials, a U.S. Department of Energy Office of Science User Facility, was supported by the U.S. DOE, Office of Basic Energy Sciences, under Contract No. DEAC02-06CH11357. The authors thank Xuedong Hu, David Schuster, and Amir Yacoby for helpful discussions.

<sup>a</sup>Email: xinhaoli@fas.harvard.edu

<sup>b</sup>Email: xzhou4@fsu.edu

<sup>c</sup>Email: dfjin@nd.edu

<sup>1</sup>X. Zhou, G. Koolstra, X. Zhang, G. Yang, X. Han, B. Dizdar, X. Li, R. Divan, W. Guo, K. W. Murch, *et al.*, “Single electrons on solid neon as a solid-state qubit platform,” *Nature* **605**, 46–50 (2022).

<sup>2</sup>X. Zhou, X. Li, Q. Chen, G. Koolstra, G. Yang, B. Dizdar, Y. Huang, C. S. Wang, X. Han, X. Zhang, *et al.*, “Electron charge qubit with 0.1 millisecond coherence time,” *Nature Physics* **20**, 116–122 (2024).

<sup>3</sup>W. Guo, D. Konstantinov, and D. Jin, “Quantum electronics on quantum liquids and solids,” *Progress in Quantum Electronics* **99**, 100552 (2024).

<sup>4</sup>A. Jennings, X. Zhou, I. Grytsenko, and E. Kawakami, “Quantum computing using floating electrons on cryogenic substrates: Potential and challenges,” *Applied Physics Letters* **124**, 120501 (2024).

<sup>5</sup>P. Platzman and M. Dykman, “Quantum computing with electrons floating on liquid helium,” *Science* **284**, 1967–1969 (1999).

<sup>6</sup>G. Burkard, T. D. Ladd, A. Pan, J. M. Nichol, and J. R. Petta, “Semiconductor spin qubits,” *Reviews of Modern Physics* **95**, 025003 (2023).

<sup>7</sup>J. R. Petta, A. C. Johnson, J. M. Taylor, E. A. Laird, A. Yacoby, M. D. Lukin, C. M. Marcus, M. P. Hanson, and A. C. Gossard, “Coherent manipulation of coupled electron spins in semiconductor quantum dots,” *Science* **309**, 2180–2184 (2005).

<sup>8</sup>F. Borsoi, N. W. Hendrickx, V. John, M. Meyer, S. Motz, F. Van Riggelen, A. Sammak, S. L. DeSnoo, G. Scappucci, and M. Veldhorst, “Shared control of a 16 semiconductor quantum dot crossbar array,” *Nature Nanotechnology* **19**, 21–27 (2024).

<sup>9</sup>L. Vandersypen, H. Bluhm, J. Clarke, A. Dzurak, R. Ishihara, A. Morello, D. Reilly, L. Schreiber, and M. Veldhorst, “Interfacing spin qubits in quantum dots and donors—hot, dense, and coherent,” *npj Quantum Information* **3**, 34 (2017).

<sup>10</sup>A. Zwerver, T. Krähenmann, T. Watson, L. Lampert, H. C. George, R. Pillarisetty, S. Bojarski, P. Amin, S. Amitonov, J. Boter, *et al.*, “Qubits made by advanced semiconductor manufacturing,” *Nature Electronics* **5**, 184–190 (2022).

<sup>11</sup>N. R. Beysengulov, Ø. S. Schøyen, S. D. Bilek, J. B. Flaten, O. Leinonen, M. Hjorth-Jensen, J. Pollanen, H. E. Kristiansen, Z. J. Stewart, J. D. Weidman, *et al.*, “Coulomb interaction-driven entanglement of electrons on helium,” *PRX Quantum* **5**, 030324 (2024).

<sup>12</sup>E. Kawakami, J. Chen, M. Benito, and D. Konstantinov, “Blueprint for quantum computing using electrons on helium,” *Physical Review Applied* **20**, 054022 (2023).

<sup>13</sup>T. Kanai, D. Jin, and W. Guo, “Single-electron qubits based on quantum ring states on solid neon surface,” *Physical Review Letters* **132**, 250603 (2024).

<sup>14</sup>X. Li, C. S. Wang, B. Dizdar, Y. Huang, Y. Wen, W. Guo, X. Zhang, X. Han, X. Zhou, and D. Jin, “Noise-resilient solid host for electron qubits above 100 mK,” *arXiv:2502.01005v2* (2025).

<sup>15</sup>K. Zheng, X. Song, and K. W. Murch, “Surface morphology assisted trapping of strongly coupled electron-on-neon charge states,” *arXiv preprint arXiv:2503.01847* (2025).

<sup>16</sup>T. Hengsens, T. Fujita, L. Janssen, X. Li, C. Van Diepen, C. Reichl, W. Wegscheider, S. Das Sarma, and L. M. Vandersypen, “Quantum simulation of a fermi-hubbard model using a semiconductor quantum dot array,” *Nature* **548**, 70–73 (2017).

<sup>17</sup>Y. Wang, Y. Chen, H. T. Bui, C. Wolf, M. Haze, C. Mier, J. Kim, D.-J. Choi, C. P. Lutz, Y. Bae, *et al.*, “An atomic-scale multi-qubit platform,” *Science* **382**, 87–92 (2023).

<sup>18</sup>D. Schuster, A. Fragner, M. Dykman, S. Lyon, and R. Schoelkopf, “Proposal for manipulating and detecting spin and orbital states of trapped electrons on helium using cavity quantum electrodynamics,” *Physical Review Letters* **105**, 040503 (2010).

<sup>19</sup>A. Blais, A. L. Grimsmo, S. M. Girvin, and A. Wallraff, “Circuit quantum electrodynamics,” *Reviews of Modern Physics* **93**, 025005 (2021).

<sup>20</sup>P. Krantz, M. Kjaergaard, F. Yan, T. P. Orlando, S. Gustavsson, and W. D. Oliver, “A quantum engineer’s guide to superconducting qubits,” *Applied Physics Reviews* **6**, 021318 (2019).

<sup>21</sup>S. Poletto, J. M. Gambetta, S. T. Merkel, J. A. Smolin, J. M. Chow, A. Córcoles, G. A. Keefe, M. B. Rothwell, J. Rozen, D. W. Abraham, *et al.*, “Entanglement of two superconducting qubits in a waveguide cavity via monochromatic two-photon excitation,” *Physical Review Letters* **109**, 240505 (2012).

<sup>22</sup>G. Koolstra, G. Yang, and D. I. Schuster, “Coupling a single electron on superfluid helium to a superconducting resonator,” *Nature Communications* **10**, 5323 (2019).

<sup>23</sup>C. Rigetti and M. Devoret, “Fully microwave-tunable universal gates in superconducting qubits with linear couplings and fixed transition frequencies,” *Physical Review B* **81**, 134507 (2010).

<sup>24</sup>E. Magesan and J. M. Gambetta, “Effective hamiltonian models of the cross-resonance gate,” *Physical Review A* **101**, 052308 (2020).

<sup>25</sup>J. M. Chow, A. D. Córcoles, J. M. Gambetta, C. Rigetti, B. R. Johnson, J. A. Smolin, J. R. Rozen, G. A. Keefe, M. B. Rothwell, M. B. Ketchen, *et al.*, “Simple all-microwave entangling gate for fixed-frequency superconducting qubits,” *Physical Review Letters* **107**, 080502 (2011).

<sup>26</sup>M. Roth, M. Ganzhorn, N. Moll, S. Philipp, G. Salis, and S. Schmidt, “Analysis of a parametrically driven exchange-type gate and a two-photon excitation gate between superconducting qubits,” *Physical Review A* **96**, 062323 (2017).

<sup>27</sup>J. Majer, J. Chow, J. Gambetta, J. Koch, B. Johnson, J. Schreier, L. Frunzio, D. Schuster, A. A. Houck, A. Wallraff, *et al.*, “Coupling superconducting qubits via a cavity bus,” *Nature* **449**, 443–447 (2007).

<sup>28</sup>S. P. Fors, J. Fernández-Pendás, and A. F. Kockum, “Comprehensive explanation of zz coupling in superconducting qubits,” arXiv preprint arXiv:2408.15402 (2024).

<sup>29</sup>J. R. Johansson, P. D. Nation, and F. Nori, “Qutip: An open-source python framework for the dynamics of open quantum systems,” Computer Physics Communications **183**, 1760–1772 (2012).

<sup>30</sup>G. Wendin, “Quantum information processing with superconducting circuits: a review,” Reports on Progress in Physics **80**, 106001 (2017).

<sup>31</sup>J.-k. Xie, R.-t. Cao, Y.-l. Ren, S.-l. Ma, R. Zhang, and F.-l. Li, “High-fidelity quantum memory with floating electrons coupled to superconducting circuits,” Physical Review A **110**, 052607 (2024).

<sup>32</sup>T. A. Baart, T. Fujita, C. Reichl, W. Wegscheider, and L. M. K. Vandersypen, “Coherent spin-exchange via a quantum mediator,” Nature Nanotechnology **12**, 26–30 (2017).

<sup>33</sup>P. Leiderer, “Surface electrons on solid quantum substrates: A brief review,” Journal of Low Temperature Physics, 1–20 (2025).

<sup>34</sup>J. Dijkema, X. Xue, P. Harvey-Collard, M. Rimbach-Russ, S. L. de Snoo, G. Zheng, A. Sammak, G. Scappucci, and L. M. Vandersypen, “Cavity-mediated iswap oscillations between distant spins,” Nature Physics **21**, 168–174 (2025).

<sup>35</sup>L. Cheung, R. Haller, A. Kononov, C. Ciaccia, J. Ungerer, T. Kanne, J. Nygård, P. Winkel, T. Reisinger, I. Pop, *et al.*, “Photon-mediated long-range coupling of two andreev pair qubits,” Nature Physics **20**, 1793–1797 (2024).

<sup>36</sup>C. Böttcher, S. Harvey, S. Fallahi, G. Gardner, M. Manfra, U. Vool, S. Bartlett, and A. Yacoby, “Parametric longitudinal coupling between a high-impedance superconducting resonator and a semiconductor quantum dot singlet-triplet spin qubit,” Nature Communications **13**, 4773 (2022).

<sup>37</sup>P. Harvey-Collard, G. Zheng, J. Dijkema, N. Samkharadze, A. Sammak, G. Scappucci, and L. M. Vandersypen, “On-chip microwave filters for high-impedance resonators with gate-defined quantum dots,” Physical Review Applied **14**, 034025 (2020).

<sup>38</sup>P. Harvey-Collard, J. Dijkema, G. Zheng, A. Sammak, G. Scappucci, and L. M. Vandersypen, “Coherent spin-spin coupling mediated by virtual microwave photons,” Physical Review X **12**, 021026 (2022).

<sup>39</sup>A. Stockklauser, P. Scarlino, J. V. Koski, S. Gasparinetti, C. K. Andersen, C. Reichl, W. Wegscheider, T. Ihn, K. Ensslin, and A. Wallraff, “Strong coupling cavity qed with gate-defined double quantum dots enabled by a high impedance resonator,” Physical Review X **7**, 011030 (2017).

<sup>40</sup>A. J. Landig, J. V. Koski, P. Scarlino, C. Müller, J. C. Abadillo-Uriel, B. Kratochwil, C. Reichl, W. Wegscheider, S. N. Coppersmith, M. Friesen, *et al.*, “Virtual-photon-mediated spin-qubit-transmon coupling,” Nature communications **10**, 5037 (2019).

<sup>41</sup>G. Koolstra, E. Glen, N. Beysengulov, H. Byeon, K. Castoria, M. Sammon, B. Dizdar, C. Wang, D. Schuster, S. Lyon, *et al.*, “High-impedance resonators for strong coupling to an electron on helium,” Physical Review Applied **23**, 024001 (2025).

<sup>42</sup>Y. Tian, I. Grytsenko, A. Jennings, J. Wang, H. Ikegami, X. Zhou, S. Tamate, H. Terai, H. Kutsuma, D. Jin, *et al.*, “NbTiN nanowire resonators for spin-photon coupling on solid neon,” arXiv preprint arXiv:2505.24303 (2025).

<sup>43</sup>X.-F. Pan and P.-B. Li, “Nonlinear tripartite coupling of single electrons on solid neon with magnons in a hybrid quantum system,” arXiv preprint arXiv:2503.08587 (2025).

## Supplemental Information for Coherent manipulation of interacting electron qubits on solid neon

### S1. RESONATOR DISPERSIVE SHIFT

$Q_1$  of the two-qubit coupled system presented in the main text is coupled to the resonator with its charge sweet-spot (SS) above the resonator frequency. Due to the interaction, the resonator is dispersively shifted when  $Q_1$  is biased close to its SS, as shown in Fig. S1a. The line-cut of the resonator spectrum when ground-state  $Q_1$  is on its SS shows  $\chi/2\pi = 0.33$  MHz red shift compared to the bare resonator frequency, as shown in Fig. S1b. We estimated the coupling strength between  $Q_1$  and resonator to be  $g_1/2\pi \approx 3.76$  MHz based on this resonator dispersive shift and  $\chi \approx g_1^2/\Delta_1$  (ref. <sup>19</sup>), where  $\Delta_1/2\pi = (\omega_1 - \omega_r)/2\pi \approx 43$  MHz.

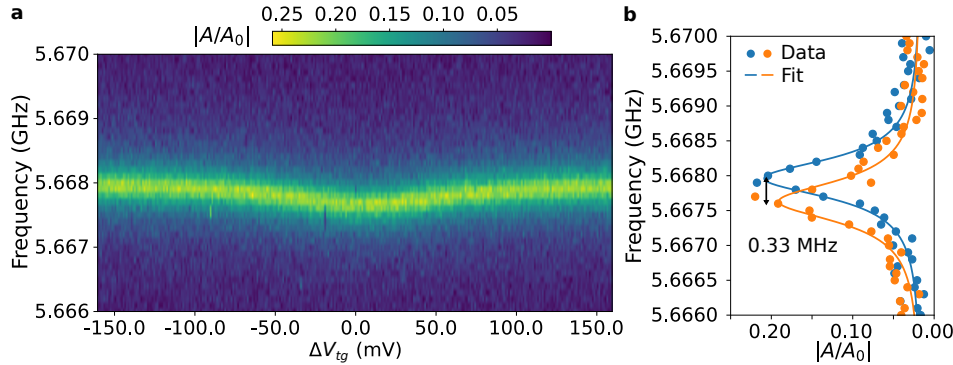


**Fig. S1. Resonator dispersive shift caused by  $Q_1$ .** **a**, Resonator spectrum probe with varying bias on trap guard, showing the dispersive shift when  $Q_1$  is close to resonator frequency. **b**, Transmission line cuts at bare resonator (blue dots and curve) and when  $Q_1$  is biased at its sweet-spot (orange dots and curve).

### S2. PULSED READOUT OF $Q_2$

We demonstrate the pulsed readout process of  $Q_2$  with the following simulation. Initially, the population of  $Q_1$  and  $Q_2$  is set to be 0 and 1, respectively. Then the resonator is populated by sending in a square readout pulse (700 ns) at the resonator frequency with varying amplitude  $\epsilon$ , as described in the Methods section. The free evolution of the coupled system is calculated with the system Hamiltonian Eq. (1) and the probing Hamiltonian Eq. (4), considering relaxation and dephasing with Eq. (3) of the main text. Figure S2 shows the evolution of intra-cavity photon number

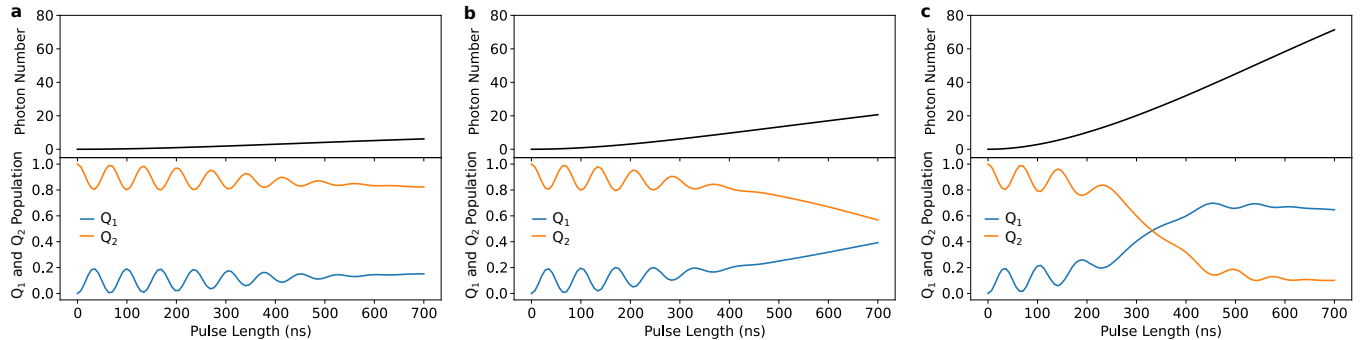


**Fig. S2. Simulation of intra-cavity photon number and qubit population evolution with varying probing amplitude.** 700 ns evolution simulated with probing amplitude  $\epsilon$  of (a) 5.6 MHz (-130 dBm reaching the resonator), (b) 10 MHz (-125 dBm reaching the resonator) and (c) 18 MHz (-120 dBm reaching the resonator), respectively. Black curves show intra-cavity photon number  $\bar{n}$ . Blue curves show  $Q_1$  population and orange curves show  $Q_2$  population.

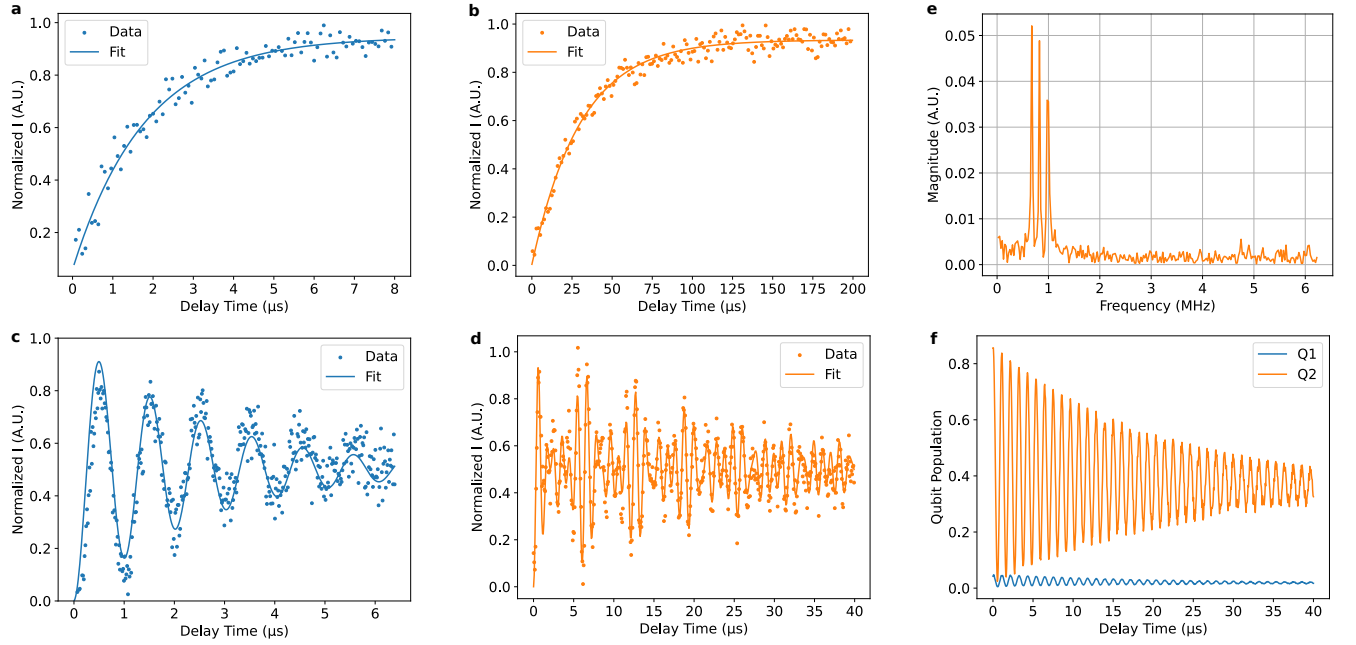


**Fig. S3. Relaxation and decoherence of Q<sub>1</sub> and Q<sub>2</sub>.** **a**, and **b**, Relaxation measurements of Q<sub>1</sub> and Q<sub>2</sub> with fitted  $T_1$  of 1.8  $\mu$ s and 30.3  $\mu$ s, respectively. **c**, and **d**, Ramsey measurements of Q<sub>1</sub> and Q<sub>2</sub> with fitted  $T_2^*$  of 2.56  $\mu$ s and 32.99  $\mu$ s, respectively. **e**, Frequency components of the Ramsey fringes in **d**, revealing frequency fluctuations of Q<sub>2</sub> during the measurement. **f**, Numerical simulation of Ramsey measurement of Q<sub>2</sub>, indicating that the beating pattern in **c** is not intrinsically caused by the coupled system.

$\bar{n}$ , Q<sub>1</sub>, and Q<sub>2</sub> excited state population under varying driving amplitude. When the probe power is small, (Fig. S2a and 2b) the ac-Stark shift of Q<sub>1</sub> caused by the probe pulse is also small, Q<sub>1</sub> and Q<sub>2</sub> weakly exchange population at high frequency approximately  $\sqrt{\Delta_{12}^2 + 4J^2}$ , where  $J$  is the inter-qubit coupling strength and  $\Delta_{12}$  are the qubits detune. With increased photon number, the blue ac-Stark shift  $2\chi\bar{n}$  causes the Q<sub>1</sub> across Q<sub>2</sub> frequency, resulting in their population swap when  $\bar{n}$  approaches 20, as shown in Fig. S2c. Further increasing the probing amplitude could populate the resonator faster and make the population swap happen even sooner. These simulation results reveal the readout process we applied to probe Q<sub>2</sub>, whose interaction strength with the resonator is small. We chose the 700 ns readout length to balance signal strength with the fast decaying of Q<sub>1</sub>, as illustrated in the following sections.

### S3. QUBITS DECOHERENCE

We evaluated Q<sub>1</sub> and Q<sub>2</sub>'s coherence via relaxation and Ramsey measurements when Q<sub>1</sub> was biased at its SS. Q<sub>1</sub> was directly driven by sending pumps through the resonator at its frequency. In contrast, Q<sub>2</sub> was driven by pumping Q<sub>1</sub> at Q<sub>2</sub>'s frequency, corresponding to the cross-resonance (CR) two-qubit operation. Q<sub>2</sub> was probed with the pulsed readout method described in the main text and the previous section. Figure S3a and S3b show the relaxation of Q<sub>1</sub> and Q<sub>2</sub> with  $T_1$  of 1.8  $\mu$ s and 30.3  $\mu$ s, respectively, fitted from the measured in-phase signal. Figure S3c shows the Ramsey fringes of Q<sub>1</sub>, with a  $T_2^*$  of 2.56  $\mu$ s fitted from the in-phase signal. The Ramsey measurement result of Q<sub>2</sub> is more complicated, as we observed multiple frequency components of the measured in-phase signal, as shown in Fig. S3d and S3e. Numerical simulation of the Ramsey measurement process with a stable single frequency of Q<sub>2</sub> reveals that the population swap between Q<sub>1</sub> and Q<sub>2</sub> induced by the inter-qubit coupling will not affect the final probed state and measured signal. Therefore, we attribute the beating features in Fig. S3d to fluctuations of the Q<sub>2</sub>'s frequency during data acquisition, which has also occurred on other qubits measured on the same device, as in ref.<sup>14</sup>. We fitted the data in Fig. S3d with a three-frequency model which resulted in a  $T_2^*$  of 32.99  $\mu$ s. The measured relaxation and decoherence rates are then used in the numerical simulation of the system.

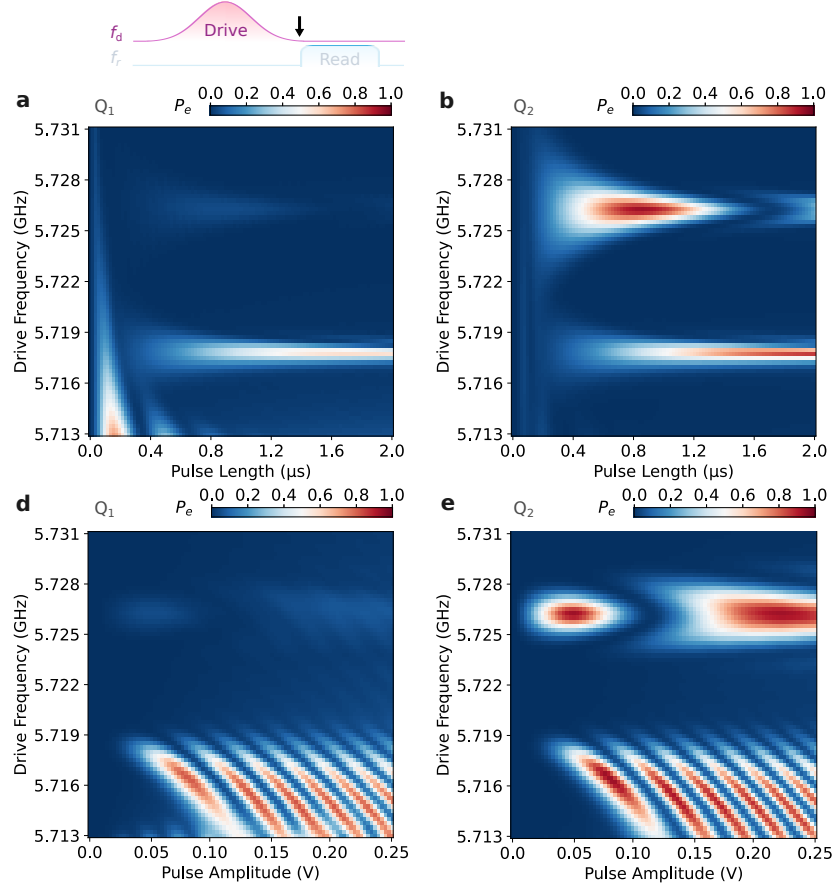
#### S4. NUMERICAL SIMULATION DETAILS

Table S1 summarizes the simulation parameters to build the Hamiltonian of the two-qubit coupled system and to account for the decoherence. Since the longitudinal interaction is small, as discussed in the main text, the  $\zeta_{12}$  term is set to be zero in the simulation. In addition, the driving amplitude  $A$  in MHz used in the simulation is scaled with  $A = 735 \times \mathcal{A}$ , where  $\mathcal{A}$  is the experimental driving pulse amplitude in V. The readout process is simulated with 700 ns square pulse with probing amplitude  $\epsilon$  at 18 MHz.

	$\omega_i/2\pi$ (GHz)	$\kappa_i/2\pi$ (MHz)	$\gamma_i/2\pi$ (MHz)	$g_i/2\pi$ (MHz)	$J_{12}/2\pi$ (MHz)
Resonator	5.668	0.38	N.A.	N.A.	N.A.
Qubit 1	5.7112	0.09	0.015	3.76	3.35
Qubit 2	5.7255	0.005	0.027	0.0	

**Tab. S1.** Summary of the simulation parameters used for the two-qubit coupled system as in Fig. 3 and 4 of the main text.

Figure S4 shows the simulated qubit excited state population before the readout process in the Rabi measurements, indicated as the arrow time stamp in the inset. The oscillation features at 5.726 GHz and 5.718 GHz, corresponding to the cross-resonance (CR) and bSWAP operation, match well with the experimental result in Fig. 3 of the main text. It confirms that the observed oscillation features are the result of the two-qubit operations instead of the probing pulse following that. In Fig. S4a and d,  $Q_2$  is excited by driving  $Q_1$  at 5.726 GHz, while the  $Q_1$ 's population barely changes. After the readout process, the  $Q_2$ 's population is swapped onto  $Q_1$ , as shown in Fig. 3b and e of the main text.



**Fig. S4. Numerical simulation of qubit excited state population before the readout process in Rabi measurements.** a and b Simulation results of  $Q_1$  (a) and  $Q_2$  (b) population after driving pulse in the pulse length-frequency Rabi measurements. c and d Simulation results of  $Q_1$  (c) and  $Q_2$  (d) population after driving pulse in the pulse amplitude-frequency Rabi measurements.

To calculate the eigenstates of the three-qubit coupled system, as in the main text Fig. 4, we modeled qubits 1, 2, and 3 with hyperbolic frequency dependency on the gate voltage  $\Delta V_{\text{res}}$  as:  $f_i = \sqrt{(\alpha_i)^2 + (\beta_i \times (\Delta V_{\text{res}} - \delta_i))^2}$ . Below, we list the parameters used to generate Fig. 4c in the main text. In addition, we used  $J_{12}/2\pi = 62.5$  MHz and  $J_{23}/2\pi = 5.0$  MHz. We also omit longitudinal interactions between qubits in the calculation.

	$\alpha_i$ (GHz)	$\beta_i$ (GHz/mV)	$\delta_i$ (mV)
Qubit 1	6.130	1.325	0.0
Qubit 2	6.135	0.218	-4.0
Qubit 3	5.915	1.30	0.08

**Tab. S2.** Summary of the simulation parameters used for the three-qubit coupled system as in Fig. 4c of the main text.

## S5. “WATERFALL” FEATURES IN PULSE AMPLITUDE-DEPENDENT RABI OSCILLATION

The “waterfall-like” pattern measured in pulse amplitude-dependent Rabi oscillation is also replicated in the numerical simulation, by realistically modeling the driving pulse with the same Gaussian envelope used in experiments. We attribute it to the combined effects of the pulse shape and ac-Stark shift of  $Q_1$  under driving at the frequency middle point between  $Q_1$  and  $Q_2$  with high power. Figure S4 plots the simulation when we replace the Gaussian-shaped driving pulse with square pulses. Under such conditions, the “waterfall-like” pattern vanishes while we could still observe the red shift of the  $|00\rangle \rightarrow |11\rangle$  transition at higher power, caused by the ac-Stark shift of  $Q_1$ .

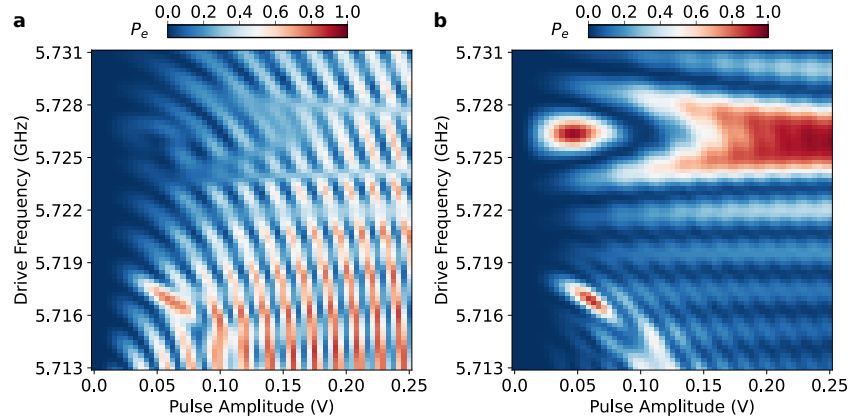


**Fig. S5. Numerical simulation of pulse amplitude-dependent Rabi oscillation with step driving pulses.** Simulation results of  $Q_1$  (a.) and  $Q_2$  (b.) population evolution, in which the “waterfall-like” pattern observed in experiments vanishes.